

Energy Efficiency of mmWave Massive MIMO Precoding with Low-Resolution DACs

Lucas N. Ribeiro, *Student Member, IEEE*, Stefan Schwarz, *Member, IEEE*, Markus Rupp, *Fellow, IEEE*, André L. F. de Almeida, *Senior Member, IEEE*

Abstract—With the congestion of the sub-6 GHz spectrum, the interest in massive multiple-input multiple-output (MIMO) systems operating on millimeter wave spectrum grows. In order to reduce the power consumption of such massive MIMO systems, hybrid analog/digital transceivers and application of low-resolution digital-to-analog/analog-to-digital converters have been recently proposed. In this work, we investigate the energy efficiency of quantized hybrid transmitters equipped with a fully/partially-connected phase-shifting network composed of active/passive phase-shifters and compare it to that of quantized digital precoders. We introduce a quantized MIMO model based on an additive quantization noise model considering a realistic power consumption and loss model to evaluate the spectral and energy efficiencies of the transmit precoding methods. Simulation results show that partially-connected hybrid precoders can be more energy-efficient compared to digital precoders, while fully-connected hybrid precoders perform poorly due to their severe insertion losses. Also, the topology of the phase-shifting components offers an energy-spectral efficiency trade-off: active phase-shifters provide higher data rates, while passive phase-shifters maintain better energy efficiency.

Index Terms—Hybrid Precoding, Millimeter Wave, Massive MIMO, Energy Efficiency, Low-Resolution DAC

I. INTRODUCTION

THE rapid increase of connected mobile terminals in the past few years has been pushing data rate requirements of 5G systems to new levels [1]. As the sub-6 GHz spectrum is congested, moving towards other ranges, such as millimeter wave (mmWave) regime, has been one of the main ideas for achieving these requirements [2]. The mmWave band is little regulated and is mostly available, allowing for mobile communication systems to operate on large bandwidths. However, the propagation characteristics on this elevated frequency range poses many engineering challenges. For instance, the path loss is very strong as it increases with the inverse of the wavelength squared. Highly directional propagation with massive antenna arrays is then required to compensate for this large path loss. Such technology has been referred to in literature as massive multiple-input multiple-output (MIMO) [3], [4].

Hybrid analog/digital (A/D) transceiver architectures have been proposed to enable mmWave massive MIMO systems [5]. They employ digital filtering (precoding/decoding) at

L. N. Ribeiro, S. Schwarz, and M. Rupp are with the Institute of Telecommunications, TU Wien, 1040 Vienna, Austria. S. Schwarz is also member of the Christian Doppler Laboratory for Dependable Wireless Connectivity for the Society in Motion, TU Wien (e-mail: {lribeiro, sschwarz, mrupp}@nt.tuwien.ac.at).

L. N. Ribeiro and A. L. F. de Almeida are with the Department of Teleinformatics Engineering, Federal University of Ceará, Fortaleza, Brazil (email: {nogueira, andre}@gtel.ufc.br).

baseband, and perform beamforming in the radio-frequency (RF) domain by analog components. The most popular implementation of this RF beamformer consists of an active phase-shifting network (PSN) connecting the outputs of the baseband filter to the antennas, which is known as fully-connected PSN. This implementation, however, is associated with a large power consumption as a considerable number of active phase-shift elements is required. As an alternative, one can employ subarray beamforming, reducing the number of phase-shifters, and, consequently, power consumption. It has been claimed that hybrid precoding provides a throughput close to that of fully-digital systems [6]. However, insertion losses of RF hardware are usually disregarded in the analysis of such hybrid systems. If these losses are not properly compensated for, then their spectral efficiency might be much smaller in practice than what is expected.

Another energy-efficient approach to mmWave massive MIMO consists of using low-resolution digital-to-analog/analog-to-digital converters (DACs/ADCs) [7]. At the receive side, the high-resolution ADC chains are the most power hungry part, motivating the application of low-resolution devices to reduce their power consumption. At the transmit side, however, power expenditure is dominated by power amplifiers (PAs), which are usually required to operate within the high linearity regime to avoid distortion of the signal constellation. Employing low-resolution DACs relaxes the linearity requirement, allowing the amplifiers to operate closer to saturation, thus increasing their efficiency.

A. Related Work

Most of recent works on massive MIMO focus on analyzing either the performance of energy-efficient full-resolution hybrid or low-resolution fully-digital transceivers. In the following, we discuss their contributions.

1) *Energy Efficiency of Hybrid Systems*: The work of [8] investigates the spectral and energy efficiencies of hybrid systems with switches and phase-shifters to perform analog beamforming. In order to evaluate energy efficiency, they define a power consumption model for both types of RF beamforming considering different interconnection of components. They also propose a channel estimation method based on compressive sensing techniques. According to simulation results, all hybrid architectures yield similar spectral efficiency for a given power consumption. In [9], the energetic performance of single/multi-carrier full-resolution hybrid transceivers is investigated. A transceiver optimization problem based on

energy efficiency maximization is presented and solved by the alternating direction of multipliers method. The power consumption model proposed therein considers the computational power expenditure and RF hardware losses, which are usually ignored in most energy efficiency models. This model assumes the application of PAs and low-noise amplifiers that compensate for the analog beamforming losses. Based on this assumption, the paper claims that hybrid precoders with fully-connected PSN can be energy-efficient, even more than those with partially-connected PSN. This conclusion, however, contradicts the results of [10], where the spectral efficiency of a hybrid precoder is examined under a realistic RF model. Therein, the fully-connected PSN is modeled as a bank of RF components described by their S-parameters. The obtained results show that SNR losses are significant, going up to 25 dB for the given scenario. Unfortunately, with the current mmWave amplifier technology, one cannot assume that these losses are simply compensated for as in [9]. Therefore, in order to make a realistic comparison between hybrid and digital transmitters, the effect of RF losses on the spectral efficiency has to be considered.

Analog and digital receivers employing low-resolution ADCs are studied in [11] for single-user MIMO (SU-MIMO). The authors resort to a stochastic linear quantization model referred to as additive quantization noise (AQN) model in order to simplify the analysis of systems with low-resolution ADCs. For digital combining, singular value decomposition (SVD) processing with water-filling power allocation is applied, whereas much simpler matched filtering is employed in analog beamforming. Lower bounds on the data rate are derived based on the linear quantization approximation, and the AQN model is shown to be accurate in the low signal-to-noise ratio (SNR) regime. Simulation results indicate that the digital combining architecture exhibits better performance than the analog scheme. The energy and spectral efficiency trade-off for digital, analog, and hybrid receivers is extensively studied in [12]. The ADC is approximated by the AQN model and achievable rate expressions are obtained. A power consumption model similar to that of [8] is considered, allowing to calculate energy efficiency. At the transmit side, the authors assume fully-digital precoding, whereas, at the receive side, fully-connected RF beamforming is employed in addition to digital baseband combining. The analog beamformers are computed by the alternating minimization method presented in [13], and the baseband filter is obtained through SVD processing with water-filling power allocation. Results indicate that analog combining is the most energy-efficient solution only at low SNR or low-rank channels, while the efficiency of hybrid and digital combining strongly depends on the assumed hardware power consumption characteristics for any other than low-rank channels. It is important to stress that [12] does not consider insertion losses at the RF domain and only investigates systems with fully-connected PSN. In [14], by contrast, hybrid receivers with partially-connected PSN are compared to digital combiners under a low-resolution ADC assumption and a multi-user MIMO (MU-MIMO) model. This contribution shows that digital receivers using low-resolution ADCs are robust to small automatic gain control (AGC) imperfection.

In the considered power consumption model, a simple implementation for a 1-bit ADC is presented, leading to negligible power consumption. The considered analog combining strategy consists of beam scanning, while baseband combining is based on SVD processing with water-filling power allocation, as in the previously mentioned works. Results suggest that digital combining is more efficient than hybrid combining especially in the low SNR regime. However, the contributions mentioned above impose low-resolution only at the receiver side, assuming fully-digital or hybrid transmitters with high-resolution DACs.

2) *Transmitters with Low-Resolution DACs*: Recently proposed massive MIMO signal processing methods such as [15], [16] assume very large antenna arrays with dedicated RF chains either at the transmit or at the receive side. However, such implementation is not energy-efficient and thus needs to be modified in order to reduce its power requirements. An alternative to hybrid systems consists of employing low-resolution DACs/ADCs at transmitter/receiver to relax the power demands on the fully-digital transceiver.

A SU-MIMO model with low-resolution quantization at the transmit side is introduced in [17]. A linear approximation for DAC quantization based on the Bussgang Theorem [18] is presented, allowing the derivation of a minimum mean square error (MMSE) precoder optimized for tackling the quantization effects. Bit error rate (BER) results reveal that this optimized MMSE filter performs better than the plain MMSE solution. In [19], a narrow-band MU-MIMO system employing low-resolution DACs at the base station is considered. The authors investigate the performance of linear precoders with coarse quantization and propose some non-linear precoders based on relaxations of the mean square error (MSE) for 1-bit signaling. Achievable rate expressions are obtained and simulation results suggest that performance achieved with infinite-resolution DAC can be attained by using 3 or 4 bits of resolution for the given scenario. Furthermore, it was shown that the presented non-linear precoding algorithms significantly outperform the linear filtering solutions for 1-bit quantization.

B. Contribution

To the best of our knowledge, extensive performance evaluation of quantized hybrid transmitters with fully- and partially-connected PSN under realistic RF modeling has not been considered yet. We thus aim at filling this gap by this paper. Our main contributions in this direction can be summarized as follows:

- A SU-MIMO system model is introduced for quantized hybrid precoding based on the AQN model. The proposed system model differs from those previously introduced in other works in the definition of the total additive noise vector, which accounts for the additive white Gaussian noise (AWGN) and an RF-filtered quantization noise.
- We define the quantized hybrid precoding problem, which can be regarded as a generalization of the quantized digital precoding and classical hybrid precoding problems. Achievable rate expressions for both schemes are

derived. For hybrid precoding, we consider both fully- and partially-connected PSNs. The effects of DAC quantization on spectral efficiency are assessed through asymptotic analysis.

- A power consumption model considering device power characteristics reported in recent literature for mmWave systems is presented. Active and passive phase-shifting topologies are considered in our model. The former has considerable power consumption and small insertion losses. By contrast, the latter has insignificant power consumption and important insertion losses. We properly account for power insertion losses in our signal model using the realistic RF modeling of [10]. The effects of signal processing computations are also considered in the power budget by the model presented in [20]. Simulations are conducted to evaluate the importance of this computational term and the obtained results suggest that it may be crucial for large-array systems.
- We introduce an analog beamforming method for partially-connected structures based on maximum eigen-mode transmission (MET), and implement this solution with the low-complexity power method of [21, Section 7.3.1]. The computational complexity of the precoding methods are determined in order to calculate their power consumption.
- The energy-spectral efficiency trade-off is investigated to determine the most efficient precoding strategy, and to study the influence of phase-shifter implementation on performance. Our results show that hybrid precoding with partially-connected PSN and digital precoding are the most energy- and spectral-efficient solutions, respectively. Fully-connected PSN, however, performs poorly due to the very large insertion losses, which cause severe spectral efficiency degradation. Moreover, we have observed that active phase-shifters favor spectral efficiency, while their passive implementations focus on energy efficiency.

This work is organized as follows: Section II describes the system model considered in this work. Signal and channel models for a narrowband mmWave SU-MIMO system are introduced therein. The quantization operation employed in DACs is defined and approximated by the AQN model, and the power consumption model is presented. The analog and digital precoding strategies adopted in this work are defined in Section III. Also, computational complexity analysis is conducted in Section III-C and achievable rate bounds are derived in Section III-D. The proposed models and precoding methods are assessed through simulations in Section IV, and the work is concluded in Section V.

C. Notation

In this paper, x denotes a scalar, \mathbf{x} a vector, and \mathbf{X} a matrix. The (i, j) -th entry of \mathbf{X} is given by $[\mathbf{X}]_{i,j}$. The transposed and conjugated transposed (Hermitian) of \mathbf{X} are denoted by \mathbf{X}^T and \mathbf{X}^H , respectively. The $(M \times M)$ -dimensional identity matrix is represented by \mathbf{I}_M . The $(M \times N)$ -dimensional null matrix is given by $\mathbf{0}_{M \times N}$. $\text{tr}(\cdot)$ is the matrix trace, $\text{diag}(\cdot)$ forms a diagonal matrix out of the main diagonal of the

matrix argument, $\text{Diag}(\cdot)$ transforms the vector input into a diagonal matrix, $\text{Diagblk}(\cdot)$ forms a block-diagonal matrix from the matrix inputs, and $\det(\cdot)$ is the determinant. The operator $\angle(\cdot)$ yields a matrix formed by the angles of each complex element of the input matrix. The absolute value, the Frobenius and ℓ_2 norms, and the expected value operator are respectively represented by $|\cdot|$, $\|\cdot\|_F$, $\|\cdot\|_2$, and $\mathbb{E}[\cdot]$. The operators $Q_b(\cdot)$ and $\mathcal{Q}_b(\cdot)$ denote scalar and vector quantization, respectively. The scalar ceiling function is given by $\lceil \cdot \rceil$. The set of circularly-symmetric jointly-Gaussian complex random vectors with mean vector $\boldsymbol{\mu}$ and covariance matrix \mathbf{C} is denoted by $\mathcal{CN}(\boldsymbol{\mu}, \mathbf{C})$.

II. SYSTEM MODEL

A. Signal Model

Consider a SU-MIMO system in which the transmitter sends N_s streams of data symbols through an array of N_t antennas to the receiver equipped with N_r antennas. The discrete-time data streams, represented by the vector $\mathbf{s} = [s_1, \dots, s_{N_s}]^T$, are assumed to be independent, Gaussian distributed with zero mean and unit variance, hence their covariance matrix is $\mathbf{R}_{ss} = \mathbb{E}[\mathbf{s}\mathbf{s}^H] = \mathbf{I}_{N_s}$. Before transmission, the data streams are precoded as $\mathbf{x} = \mathcal{P}(\mathbf{s}) \in \mathbb{C}^{N_t}$ satisfying the average power constraint $P_x = \mathbb{E}[\|\mathbf{x}\|_2^2] \leq P_{\max}$, where $\mathcal{P}(\cdot) : \mathbb{C}^{N_s} \rightarrow \mathbb{C}^{N_t}$ represents the precoding operator. The propagation channel is assumed to be narrow-band block-fading, so there is no inter-symbol interference, and the discrete-time representation of the received signal can be expressed as

$$\mathbf{y} = \mathbf{H}\mathbf{x} + \mathbf{n} \in \mathbb{C}^{N_r}, \quad (1)$$

where $\mathbf{H} \in \mathbb{C}^{N_r \times N_t}$ denotes the MIMO channel matrix, and $\mathbf{n} \sim \mathcal{CN}(\mathbf{0}_{N_r \times 1}, \sigma_n^2 \mathbf{I}_{N_r})$ is the AWGN vector. The SNR normalized with respect to the maximum average transmit power is defined as $\gamma = P_{\max}/\sigma_n^2$.

We consider digital and hybrid A/D precoding schemes. The former consists of precoding the data streams using only a digital baseband filter $\mathbf{F}_{\text{BB}} \in \mathbb{C}^{N_t \times N_s}$, which feeds signals to N_t DAC/RF chain pairs connected PAs and then to the antennas, as illustrated in Figure 1a. The latter scheme aims at decreasing the precoding power consumption by employing only $L_t < N_t$ DAC/RF chain pairs. To achieve this, the data streams are first precoded by a digital baseband precoder $\mathbf{F}_{\text{BB}} \in \mathbb{C}^{L_t \times N_s}$, which feeds L_t DAC/RF chain pairs. Next, the up-converted signals are filtered by an analog precoder, amplified and transmitted through the antenna array. We consider that the analog beamforming is implemented by low-resolution phase-shifters as in [22]. Fully- and partially-connected PSN topologies are considered for analog beamforming. In fully-connected PSNs, the output of each RF chain is divided by N_t -port power dividers and connected to N_t phase-shifters. Afterwards, the shifted signals are combined by L_t -port power combiners at each PA/antenna pair. In this case, the analog precoder is represented by a full matrix $\mathbf{F}_{\text{RF}} \in \mathbb{C}^{N_t \times L_t}$ whose entries are constrained to have unit modulus and discrete phase resolution, i.e., $[\mathbf{F}_{\text{RF}}]_{m,n} \in \mathcal{F}_{\text{RF}}$, $m \in \{1, \dots, N_t\}$, $n \in \{1, \dots, L_t\}$. The set $\mathcal{F}_{\text{RF}} = \{1, \phi, \phi^2, \dots, \phi^{n_{\text{ps}}-1}\}$ denotes the phase-shift set,

$\phi = \exp(j2\pi/n_{\text{PS}})$ the angular resolution, $n_{\text{PS}} = 2^{b_{\text{PS}}}$ the number of phase-shifts supported by the hardware, and b_{PS} the bit resolution. This architecture employs in total $L_t N_t$ phase-shift elements and is illustrated in Figure 1b. In partially-connected PSNs, by contrast, each RF chain is linked to only a sub-array of $N_a = \lceil N_t / L_t \rceil$ phase-shifters directly connected to PA/antenna pairs, as illustrated in Figure 1c. Therefore, the PSN for this architecture employs only N_a -port power dividers and no power combiners at all. The analog beamforming matrix in this case presents the following structure: $\mathbf{F}_{\text{RF}} = \text{Diagblk}(\mathbf{f}_1, \dots, \mathbf{f}_{L_t}) \in \mathbb{C}^{N_t \times L_t}$, where $\mathbf{f}_\ell \in \mathbb{C}^{N_a}$ denotes the analog beamforming filter of the ℓ -th sub-array. The phase-shifters constrain the sub-arrays analog beamforming filters as $[\mathbf{f}_\ell]_m \in \mathcal{F}_{\text{RF}}$, $\ell = 1, \dots, L_t$, $m \in \{1, \dots, N_a\}$.

To make our model consistent with power constraints present in real-world implementations, we incorporate nonlinearities due to the DAC stages and RF losses caused by analog beamforming. The non-linearity introduced by DACs is modeled as a quantization stage. This is because the continuous-valued DAC output signal has its amplitude well-represented by a finite set of values generated by the DAC hold circuits. The RF losses are accounted by considering a power loss factor $\frac{1}{\sqrt{L_{\text{RF}}}}$ multiplying the analog beamforming matrix \mathbf{F}_{RF} . The insertion loss of the analog precoder is represented by L_{RF} and depends on the power characteristics of the dividers, combiners and phase-shifters, as proposed in [10]. This insertion loss is further detailed in Section II-D. To include DAC and RF losses into our model, we define the precoding operation as

$$\mathbf{x} = \frac{1}{\sqrt{L_{\text{RF}}}} \mathbf{F}_{\text{RF}} \mathcal{Q}_b(\mathbf{F}_{\text{BB}} \mathbf{s}) = \frac{1}{\sqrt{L_{\text{RF}}}} \tilde{\mathbf{x}}, \quad (2)$$

where $\mathcal{Q}_b(\cdot)$ stands for the vector quantization operator with b bits of resolution per dimension, and $\tilde{\mathbf{x}} = \mathbf{F}_{\text{RF}} \mathcal{Q}_b(\mathbf{F}_{\text{BB}} \mathbf{s})$ the lossless transmitted signal. The vector operator will be further detailed and linearly approximated in Section II-B. Notice that (2) refers to digital precoding by setting $\mathbf{F}_{\text{RF}} = \mathbf{I}_{N_t}$, $L_{\text{RF}} = 1$, and $\mathbf{F}_{\text{BB}} \in \mathbb{C}^{N_t \times N_s}$. Therefore, for notation convenience, we consider that the quantization input and output vectors are M -dimensional, where $M = N_t$ and $M = L_t$ for digital and hybrid precoding, respectively. Thus \mathbf{F}_{RF} and \mathbf{F}_{BB} are $(N_t \times M)$ and $(M \times N_s)$ -dimensional, respectively.

B. Quantized Signal Model

Let us define the quantization operation in this work to model DAC and introduce its linear approximation. We define $\mathcal{Q}_b(\cdot)$ as the uniform scalar quantizer that operates independently on both real and imaginary components of the input. A quantizer with b resolution bits has $N_b = 2^b$ codes for representing the quantized values. The quantizer output is $p = \mathcal{Q}_b(u) = c_i^R + j c_\ell^I$ when $\Re{e}[u] \in [a_{i-1}, a_i]$ and $\Im{m}[u] \in [b_{\ell-1}, b_\ell]$, for $i, \ell \in \{1, \dots, N_b - 1\}$. The value c_i^R (c_ℓ^I) represents the code associated with the real (imaginary) part of the i -th (ℓ -th) quantization interval, and a_i (b_ℓ) the quantization segment for the real (imaginary) component. We set $a_0 = b_0 = -\infty$ and $a_{N_b-1} = b_{N_b-1} = \infty$ to support inputs with arbitrary power. The quantization codes are chosen to minimize the MSE of Gaussian distributed signals, and they

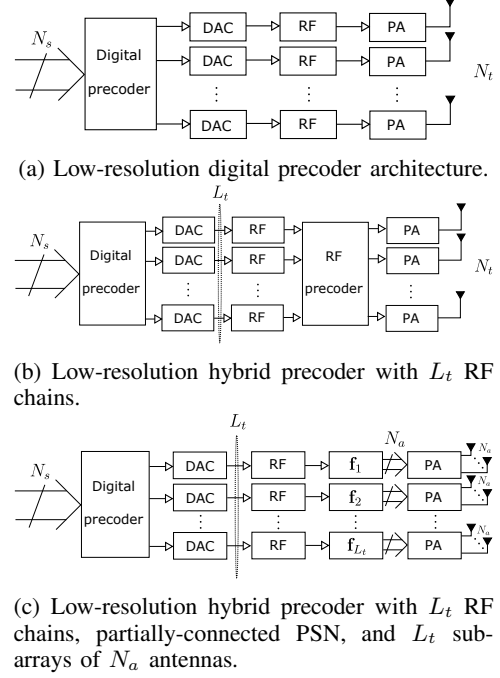


Fig. 1: Transmitter architectures considered in this work.

are listed in [23, Table II]. Such coding suits our modeling since the baseband precoded signals are still Gaussian. For vector inputs, we define $\mathcal{Q}_b(\cdot) : \mathbb{C}^M \rightarrow \mathbb{C}^M$ such that $\mathbf{p} = \mathcal{Q}_b(\mathbf{u}) \Rightarrow [\mathbf{y}]_m = \mathcal{Q}_b([\mathbf{x}]_m)$, $m \in \{1, \dots, M\}$. The vector quantizer simply consists of applying scalar quantization to each input vector entry. Unlike the Lloyd-Max quantizer [24], the considered vector quantization approach is not optimal in the MSE sense.

Conducting performance analysis of a MIMO system in terms of the exact non-linear quantization model presented above would be challenging. Among many reasons, we can point to the difficulty of calculating the statistics of the transmitted signals. As alternative, we resort to a linear approximation of the scalar quantizer output applying the AQN model [11], [12], [25] $p = \mathcal{Q}_b(u) \approx \sqrt{1 - \rho_b} u + e$. The input u is assumed to be Gaussian distributed, e is the quantization noise uncorrelated with u , and ρ_b is a quantization distortion factor, which is defined as the ratio of the quantization noise variance $\sigma_e^2 = \mathbb{E}[|e|^2]$ and the input signal variance $\sigma_u^2 = \mathbb{E}[|u|^2]$, i.e., $\rho_b = \sigma_e^2 / \sigma_u^2$ [25]. Values for this factor are listed in [23, Table II, page 12] for bit resolution up to 5 bits. For larger resolution, it can be approximated as $\rho_b = \frac{\pi\sqrt{3}}{2} 2^{-2b}$ [25]. Note that the quantization distortion factor also represents the inverse of the signal-to-quantization-noise ratio (SQNR). Thus, when the SQNR goes to infinity, the bit resolution b increases and ρ_b converges to zero. In this quantization model, the additive noise power is proportional to the input variance and decreases as the quantization resolution grows. Such a behavior is coherent with practice and motivates the adoption of this model. Also note that the approximation definition ensures that $\sigma_p^2 = \sigma_u^2$. Let us extend the AQN model to MIMO systems:

$$\mathbf{p} = \mathcal{Q}_b(\mathbf{u}) \approx \mathbf{\Upsilon}_b \mathbf{u} + \mathbf{e} \in \mathbb{C}^M. \quad (3)$$

Vectors $\mathbf{u} = [u_1, \dots, u_M]^\top$ and $\mathbf{p} = [p_1, \dots, p_M]^\top$ denote respectively the input and output of the quantizer, and $\mathbf{e} = [e_1, \dots, e_M]^\top$ the noise quantization vector which satisfies $\mathbb{E}[\mathbf{u}\mathbf{e}^\top] = \mathbb{E}[\mathbf{e}\mathbf{u}^\top] = \mathbf{0}_{M \times M}$. The diagonal matrix $\mathbf{\Upsilon}_b = \text{Diag}(\sqrt{1 - \rho_{b,1}}, \dots, \sqrt{1 - \rho_{b,M}})$ is formed by the quantization distortion factors $\rho_{b,m}$ associated with the m -th quantizer input-output. From the definition of ρ_b , it follows that the covariance matrix of the quantization error vector is given by:

$$\mathbf{R}_{ee} = \text{Diag}(\rho_{b,1}, \dots, \rho_{b,M}) \text{diag}(\mathbf{R}_{uu}) \in \mathbb{C}^{M \times M}, \quad (4)$$

where $\mathbf{R}_{uu} = \mathbb{E}[\mathbf{u}\mathbf{u}^\top]$ denotes the quantizer input covariance matrix. Knowledge of these covariance matrices will be useful in Section III, where we will derive the achievable rate for each precoder.

The AQN model approximates a non-linear deterministic operation as a linear stochastic process by assuming zero correlation between the quantizer input and the quantization noise. Similar results are obtained by using the Bussgang Theorem [18], which states that the cross-correlation function between two Gaussian signals taken after one of them has been non-linearly distorted is proportional to the cross-correlation function before distortion. If a linear model, e.g. (3), is used to approximate the non-linear distortion, this Theorem implies that the approximation error is uncorrelated with the input, i.e., $\mathbb{E}[\mathbf{u}\mathbf{e}^\top] = \mathbb{E}[\mathbf{e}\mathbf{u}^\top] = \mathbf{0}_{M \times M}$. Therefore, the Bussgang Theorem can be seen as the theoretical foundation underlying the AQN model, since this non-correlation assumption is crucial. It was shown in [14] that AGC error could invalidate this assumption, but errors between -20% and 20% are still acceptable. Model accuracy has been investigated in [11] and it was found to be very accurate in the low SNR regime, provided that the input signals are Gaussian distributed.

Now let us apply the AQN model to the precoded signal model (2). Define the the DAC input signal $\mathbf{u} = \mathbf{F}_{BBS} \in \mathbb{C}^M$. The lossless transmitted signal defined in (2) can now be approximated as

$$\tilde{\mathbf{x}} \approx \mathbf{F}_{RF} \mathbf{\Upsilon}_b \mathbf{u} + \mathbf{F}_{RFE} \in \mathbb{C}^{N_t}. \quad (5)$$

Since the data streams $\{s_1, \dots, s_{N_s}\}$ are Gaussian distributed, the baseband precoded signal $\{u_1, \dots, u_M\}$ will also be Gaussian distributed with covariance matrix $\mathbf{R}_{uu} = \mathbf{F}_{BB} \mathbf{F}_{BB}^\top$. As each quantizer output is Gaussian distributed and has b bits of resolution, it is reasonable to claim that all DACs yield the same distortion ρ_b , i.e., $\rho_{b,1} = \rho_{b,2} = \dots = \rho_{b,M} = \rho_b$, and, consequently, it follows that $\mathbf{\Upsilon}_b = \sqrt{1 - \rho_b} \mathbf{I}_M$. Now the error covariance matrix (4) can be simply expressed as

$$\mathbf{R}_{ee} = \rho_b \text{diag}(\mathbf{R}_{uu}). \quad (6)$$

Using (2) and (5), the received signal model (1) can be approximated as:

$$\mathbf{y} = \mathbf{H}\mathbf{x} + \mathbf{n} \approx \frac{1}{\sqrt{L_{RF}}} \mathbf{H}' \mathbf{u} + \mathbf{n}', \quad (7)$$

where $\mathbf{H}' = \mathbf{H}_{eq} \mathbf{\Upsilon}_b$ denotes the $(N_r \times M)$ -dimensional total channel matrix, $\mathbf{H}_{eq} = \mathbf{H}\mathbf{F}_{RF} \in \mathbb{C}^{N_r \times M}$ the equivalent channel formed by the cascade of the analog precoding and the transmission channel, and $\mathbf{n}' = \frac{1}{\sqrt{L_{RF}}} \mathbf{H}_{eq} \mathbf{e} + \mathbf{n} \in \mathbb{C}^{N_r}$

the total additive noise component. The total channel matrix \mathbf{H}' is formed by the cascade of \mathbf{H}_{eq} and the quantization scaling $\mathbf{\Upsilon}_b$. The former factor models the effect of the physical channel \mathbf{H} and the lossless analog precoder \mathbf{F}_{RF} (for hybrid structures). Of course, one must have already designed \mathbf{F}_{RF} to form \mathbf{H}_{eq} , and, indeed, computing \mathbf{F}_{RF} is the first step of the hybrid precoding strategies we present in Section III. The factor $\mathbf{\Upsilon}_b$, on the other hand, reflects the reduction of the useful transmit power due to quantization. For high-resolution quantization, $\rho_b \rightarrow 0$ and $\mathbf{H}' \rightarrow \mathbf{H}_{eq}$, thus, in this case, the quantization noise has no impact on the total channel power. By contrast, for low- and mid-resolution quantization, $\mathbf{\Upsilon}_b$ becomes important and the total channel is then expressed as $\mathbf{H}' = (1 - \rho_b) \mathbf{H}_{eq}$. Since $(1 - \rho_b)$ is always smaller than one, low-resolution quantization decreases the total channel power. Another interesting feature of model (7) is that \mathbf{n}' comprises the AWGN plus an attenuated channel-filtered quantization noise term. Therefore, \mathbf{n}' is not guaranteed to be Gaussian, as nothing is assumed about the distribution of \mathbf{e} . The covariance matrix of the total additive noise is

$$\mathbf{R}_{n'n'} = \mathbb{E}[\mathbf{n}' \mathbf{n}'^\top] = \frac{1}{L_{RF}} \mathbf{H}_{eq} \mathbf{R}_{ee} \mathbf{H}_{eq}^\top + \mathbf{R}_{nn} \in \mathbb{C}^{N_r \times N_r}, \quad (8)$$

where $\mathbf{R}_{nn} = \sigma_n^2 \mathbf{I}_{N_r}$, and the quantization noise covariance matrix \mathbf{R}_{ee} is given by Equation (6). One can easily see that $\mathbf{R}_{n'n'}$ is in general not a diagonal matrix, therefore the total additive noise vector entries are correlated. Note that we assume $\mathbb{E}[\mathbf{n} \mathbf{n}^\top] = \mathbf{0}_{N_r \times N_r}$, which is reasonable in practice, since the quantization process at the transmitter has no influence whatsoever on the receiver sensor noise.

Unfortunately, Equation (7) is still problematic when it comes to obtaining achievable rate expressions. It is difficult to separate the total MIMO channel \mathbf{H}' into orthogonal subchannels due to the structure of the total noise vector \mathbf{n}' . There are no guarantees that \mathbf{n}' is Gaussian distributed, complicating the achievable rate maximization. Moreover, its covariance matrix (8) depends on \mathbf{R}_{ee} , which varies according to the diagonal elements of \mathbf{R}_{uu} , bringing a causality problem for the precoder design. In view of these difficulties, we make some assumptions to simplify our analysis and to obtain a lower-bound for the achievable rate. In [26], it was shown that the Gaussian noise distribution minimizes the mutual information for a given noise covariance matrix. This result motivates us to approximate the additive quantization noise \mathbf{n}' as a jointly Gaussian distributed noise vector $\mathbf{n}_G = \frac{1}{\sqrt{L_{RF}}} \mathbf{H}_{eq} \mathbf{e} + \mathbf{n}$ with covariance matrix $\mathbf{R}_{n_G n_G} = \mathbf{R}_{n'n'}$. The received signal model (7) can now be approximated as $\mathbf{y} \approx \frac{1}{\sqrt{L_{RF}}} \mathbf{H}' \mathbf{u} + \mathbf{n}_G$. In order to obtain the achievable rate lower-bound, the colored noise vector \mathbf{n}_G needs to be decorrelated. Since $\mathbf{R}_{n_G n_G}$ is a Hermitian matrix, it admits an eigenvalue decomposition $\mathbf{R}_{n_G n_G} = \mathbf{J} \mathbf{L} \mathbf{J}^\top$, where $\mathbf{J}^\top \mathbf{J} = \mathbf{J} \mathbf{J}^\top = \mathbf{I}_{N_r}$. The whitening filter is thus given by $\mathbf{R}_{n_G n_G}^{-1/2} = \mathbf{L}^{-1/2} \mathbf{J}^\top$ [27], and the received signal \mathbf{y} is pre-multiplied by this filter, yielding:

$$\mathbf{R}_{n_G n_G}^{-1/2} \mathbf{y} = \frac{1}{\sqrt{L_{RF}}} \mathbf{R}_{n_G n_G}^{-1/2} \mathbf{H}' \mathbf{u} + \mathbf{R}_{n_G n_G}^{-1/2} \mathbf{n}_G. \quad (9)$$

Notice that after noise whitening, the covariance matrix of the noise vector in (9) is an $(N_r \times N_r)$ -dimensional identity matrix. We further apply model (9) in Section III to define the quantized hybrid precoding problem.

C. Channel Model

Experiments conducted in [28], [29] indicate that mmWave massive MIMO channels present a high degree of spatial and angular sparsity due to the large path loss, and thus there are only a few dominant multipaths. Such channels can be modeled by a narrow-band clustered channel model contributing with L propagation paths [6], [7] resulting in a channel matrix:

$$\mathbf{H} = \sqrt{\frac{N_t N_r}{L}} \sum_{\ell=1}^L \alpha_\ell \mathbf{a}_r(\theta_\ell^r, \phi_\ell^r) \mathbf{a}_t(\theta_\ell^t, \phi_\ell^t)^\text{H} \in \mathbb{C}^{N_r \times N_t}, \quad (10)$$

where $\alpha_\ell \in \mathbb{C}$ denotes the small-scale fading, $\mathbf{a}_r(\theta_\ell^r, \phi_\ell^r) \in \mathbb{C}^{N_r}$ and $\mathbf{a}_t(\theta_\ell^t, \phi_\ell^t) \in \mathbb{C}^{N_t}$ the array response and steering vectors evaluated at elevation θ_ℓ^r (θ_ℓ^t) and azimuth ϕ_ℓ^r (ϕ_ℓ^t) arrival (departure) angles at the receiver (transmitter), respectively. Each channel matrix realization is normalized such that $\mathbb{E} [\|\mathbf{H}\|_\text{F}^2] = N_r N_t$. We assume that each path has the same average power, i.e., α_ℓ is modeled as circular symmetric Gaussian random variables with zero mean and unit variance. The departure/arrival elevation and azimuth angles are uniformly distributed in the interval $]-\pi/2, \pi/2[$ and $[0, 2\pi]$ radians, respectively.

The transmit and receive arrays are assumed to be linear and uniformly spaced with inter-element spacing $d = \lambda/2$. The methods discussed in this paper could be easily applied to arbitrary array geometries. Under the uniform linear array (ULA) assumption, the steering and array response vectors follow the Vandermonde structure $\mathbf{a}_z(\theta) = \frac{1}{\sqrt{N_z}} [1, \dots, e^{j\pi(N_z-1)\cos\theta}]^\text{T} \in \mathbb{C}^{N_z}$, for $z \in \{t, r\}$.

D. Power Consumption and Loss Models

Energy efficiency is an important concern in the design of mmWave massive MIMO systems. Large antenna arrays are employed to compensate for the increased path loss of mmWave channels and to achieve high spectral efficiency. However, several electronic components such as DACs, phase-shifters, and power amplifiers become inefficient when operating in the millimeter wave range over large bandwidth, making radio systems equipped with such arrays expensive due to large power consumption and losses of their RF front-end. Therefore, there has been important research efforts on designing systems that not only maximize its spectral efficiency, but also its energy efficiency, which can be defined as the ratio between the system capacity and its power consumption [20].

Hybrid systems decrease power consumption by employing only a few RF chains and an analog beamforming stage. Although a hybrid architecture exhibits reduced power consumption compared to fully-digital systems in general, it also presents important power losses due to phase-shifters, and power dividers and combiners. To compensate for these losses, one could simply adopt high-gain PAs that would cover the insertion losses. However, high-gain and high-efficiency PAs are not available for mmWave yet, and, thus, these losses cannot be easily compensated, incurring in spectral efficiency degradation. In order to consider these power losses in our modeling, we adopt the realistic RF formulation introduced in

[10] which is based on the S-parameter representation of the RF hardware.

Recently, active and passive phase-shifting elements for mmWave have been reported in [30]. The former present non-negligible power consumption and relatively small insertion loss, whereas the latter has almost zero power consumption and considerable insertion loss. Therefore, the system designer can either maximize spectral efficiency with increased power consumption active phase-shifters, or reduce power consumption with decreased spectral efficiency. Which phase-shifter implementation leads to the most energy-efficient hybrid A/D system is not clear. Therefore, in order to compare the performance of the different transmitting architectures, we define power consumption models, and we introduce the power loss modeling of [10] in the following.

The influence of signal processing on the system power consumption may be important in massive MIMO systems. It is well-known that standard signal processing methods significantly increase their computational demand as the number of antennas grows. Since these methods use dedicated powerful devices for carrying out this processing, it is a good idea to avoid extensive computations in order to save energy. As pointed out in [31], this aspect is usually overlooked and should be considered during system optimization. Therefore, in our modeling, we consider a *computational* term corresponding to the power cost resulting from the calculations carried out by a given precoding method, and a *static* power consumption term, which corresponds to the cost of maintaining the RF front-end of a specific architecture.

Let us first discuss the static power consumption of hybrid and digital transmitters. The transmitter RF front-end is formed by DACs for each I/Q channel, RF chains, PSN (hybrid systems), and PAs. The considered direct conversion RF chain consists of two low-pass filters, two mixers, a local oscillator (LO) shared among all chains, and a 90° hybrid with buffers. Denoting the power consumption of low-pass filter, mixer, local oscillator, hybrid with buffer as P_{LP} , P_{M} , P_{LO} , P_{H} , respectively, the power consumption P_{RF} of a single RF chain is then

$$P_{\text{RF}} = 2P_{\text{LP}} + 2P_{\text{M}} + P_{\text{H}}. \quad (11)$$

A transmitter with digital precoding employs N_t RF chains, power amplifiers, and pairs of DACs, thus its power consumption is given by $P_{\text{D}}(N_t, b_{\text{DAC}}, F_s) = P_{\text{LO}} + P_{\text{PA}} + N_t[2P_{\text{DAC}}(b_{\text{DAC}}, F_s) + P_{\text{RF}}]$, where P_{LO} , and $P_{\text{DAC}}(b_{\text{DAC}}, F_s)$ denote power consumption of a single local oscillator, and DAC with b_{DAC} bits of resolution sampling at F_s Hertz, respectively. P_{PA} stands for the power consumed by all PAs. A hybrid transmitter with fully-connected PSN, by contrast, employs L_t DAC/RF chain pairs, and N_t power amplifiers. A total of $N_t L_t$ phase-shifters are used in this architecture, thus the total power consumption is $P_{\text{EPSN}}(N_t, L_t, b_{\text{DAC}}, b_{\text{PS}}, F_s) = P_{\text{LO}} + P_{\text{PA}} + L_t[2P_{\text{DAC}}(b_{\text{DAC}}, F_s) + P_{\text{RF}}] + N_t L_t P_{\text{PS}}(b_{\text{PS}})$, where P_{PS} denotes power consumption of a single phase-shift element with b_{PS} bits of resolution. In general, the power consumption of dividers and combiners is negligible. Transmitters with partially-connected PSN have N_a phase-shifters per sub-array, i.e., there are $N_a L_t$ phase-shifters in total, hence their

power consumption is given by $P_{\text{PPSN}}(N_t, L_t, b_{\text{DAC}}, b_{\text{PS}}, F_s) = P_{\text{LO}} + P_{\text{PA}} + L_t[2P_{\text{DAC}}(b_{\text{DAC}}, F_s) + P_{\text{RF}}] + N_a L_t P_{\text{PS}}(b_{\text{PS}})$.

The need of efficient mmWave systems fueled the development of new electronic components. One can find in the literature different parameters for the electronic devices considered in our models. We adopt an optimistic parameter selection approach, in which we choose the most efficient implementation reported. Results obtained with this approach ought to provide an idea of what to expect for future mmWave massive MIMO systems. Regarding the power consumption of the RF chain components, we consider values reported in [32, Chapter 5] for the 90° hybrid with buffers, [33] for the mixers, [34] for the low-pass filters, and [35] for the LO. We employ DACs with a binary-weighted current-steering topology. Its power consumption is a function of the effective number of bits b_{DAC} and the sampling frequency F_s [36]:

$$P_{\text{DAC}} = 1.5 \times 10^{-5} \cdot 2^{b_{\text{DAC}}} + 9 \times 10^{-12} \cdot b_{\text{DAC}} \cdot F_s. \quad (12)$$

Equation (12) was obtained by the same parameter setup as in [36]. According to [37, Section 1], this type of DAC is well-adapted for high-speed conversion since no buffer is required and thus switching can be done very fast. PAs are the most power hungry devices on the transmit side, because the high linearity requirements render them inefficient. The power consumed by the set of PAs with power-added efficiency (PAE) η is given by $P_{\text{PA}} = P_x/\eta$ [38], where P_x is the actual transmit power considering RF losses defined in Section III. Peak PAE values for state-of-art PAs are listed in [39], and vary between 6.5–27%. According to our optimistic approach, we set $\eta = 27\%$. State-of-art mmWave active phase-shifters have been listed in [8]. Their power consumption lies in the range 15–108 mW and they exhibit a low insertion loss. As alternative to active phase-shifters, passive implementations with negligible power consumption, and significant power loss have been reported in [30]. We spend $P_{\text{PS}} = 21.6$ mW for active phase-shifters [40] and consider zero power consumption for passive phase-shifters [30]. The assumed power consumption values of the RF front-end components are summarized in Table I.

Let us now present the power loss model considered in this work. In [10], the fully-connected PSN was represented in terms of elementary RF components and described in terms of their S-parameters. It is shown that power losses lead to the following representation of the analog precoding matrix:

$\mathbf{F}_{\text{RF}}/\sqrt{L_{\text{RF}}^{\{\text{FPSN}, \text{PPSN}\}}}$, where $L_{\text{RF}}^{\{\text{FPSN}, \text{PPSN}\}}$ denotes the loss factor due to insertion losses for fully- and partially-connected analog precoders. Since fully-connected PSNs employ N_t -port power dividers, and L_t -port power combiners, the corresponding loss factor is given by $L_{\text{RF}}^{\text{FPSN}} = L_{\text{PS}} \cdot L_{\text{D}}(N_t) \cdot L_{\text{C}}(L_t) \cdot N_t \cdot L_t$, where L_{PS} , $L_{\text{D}}(N_t)$, and $L_{\text{C}}(L_t)$ denote the static power loss introduced by each phase-shifter (active or passive), the loss of all N_t -port power dividers, and L_t -port combiners, respectively [10]. Partially-connected PSNs, however, use only N_a -port power dividers, yielding $L_{\text{RF}}^{\text{PPSN}} = L_{\text{PS}} \cdot L_{\text{D}}(N_a) \cdot N_a$. We consider that K -port power combiners and dividers are formed by concatenating $\lceil \log_2(K-1) \rceil$ three-port devices as in [10], thus the static loss for the total dividing and combining

Table I: Power consumption and loss of the RF front-end components.

Component	Notation	Value
Power amplifier [39]	P_{PA}	$P_x/\eta, \eta = 27\%$
Phase-shifter (active [40] ; passive [30])	P_{PS}	21.6 ; 0 mW
DAC (Equation (12)) [36]	P_{DAC}	Eq. (12)
Local oscillator [35]	P_{LO}	22.5 mW
90° hybrid with buffers [32]	P_{H}	3 mW
Mixer [33]	P_{M}	0.3 mW
LP filter [34]	P_{LP}	14 mW
RF chain (Equation (11))	P_{RF}	31.6 mW
Three-port power divider [10]	\bar{L}_{D}	0.6 dB
Three-port power combiner [10]	\bar{L}_{C}	0.6 dB
Phase-shifter (active [40] ; passive [30])	L_{PS}	2.3 ; 8.8 dB

stages is given by $L_{\{\text{D}, \text{C}\}}(K) [\text{dB}] = \bar{L}_{\{\text{D}, \text{C}\}} [\log_2(K-1)]$. Values for L_{PS} , \bar{L}_{D} , and \bar{L}_{C} are listed in Table I.

The computational analysis of precoding methods, which is based on numerical linear algebra, involves counting of arithmetical operations, memory overhead analysis, among other factors [21]. Here, we consider the computational power consumption model introduced in [20], in which the power spent with numerical calculations is proportional to the number N_{flops} of floating-point operations (flops) demanded by the algorithm, the number C of coherence blocks per second, and inversely proportional to the transmitter computational efficiency E_c [flops/s/W], i.e., it is given by $P_{\text{comp}} = C N_{\text{flops}} / E_c$. The number C of coherence blocks determines how many times the system has to update its precoding filters per second. Naturally, the computational power consumption in practice strongly depends on the hardware implementation. However, distinct implementations are characterized by different computational efficiency E_c . Therefore, the considered model is general enough to provide insights on the computational power consumption at the transmitter.

III. PRECODING STRATEGIES

In this section, we introduce the quantized hybrid precoding problem, and present precoding strategies to solve it. Analog precoding methods for FPSN and PPSN are presented in Sec. III-A, baseband precoding is defined in Sec. III-B, computational complexity analysis is conducted in Sec. III-C, and achievable rate lower bounds are derived in Sec. III-D.

The *quantized hybrid precoding problem* is based on system model (9) assuming channel state information at the transmitter (CSIT). It consists of finding the precoding matrices \mathbf{F}_{RF} and \mathbf{F}_{BB} that maximize the achievable instantaneous rate R [41], i.e.,

$$\begin{aligned} & \underset{\mathbf{F}_{\text{RF}}, \mathbf{F}_{\text{BB}}}{\text{maximize}} \quad \log_2 \det \left(\mathbf{I}_{N_r} + \frac{1}{L_{\text{RF}}} \mathbf{R}_{n_G n_G}^{-1/2} \mathbf{H}' \mathbf{R}_{uu} \mathbf{H}^H \mathbf{R}_{n_G n_G}^{-1/2, H} \right) \\ & \text{subject to} \quad [\mathbf{F}_{\text{RF}}]_{u,v} \in \mathcal{F}_{\text{RF}}, \forall u \forall v, \mathbb{E} [\|\tilde{\mathbf{x}}\|_2^2] \leq P_{\text{max}}. \end{aligned} \quad (13)$$

The capacity expression in (13) provides some insights on the performance of the quantized hybrid precoder. In order to discuss them, consider the actual transmitted power

$P_x = \mathbb{E}[\|\mathbf{x}\|_2^2] = \frac{1}{L_{\text{RF}}} P_{\tilde{x}}$, where $P_{\tilde{x}} = \mathbb{E}[\|\tilde{\mathbf{x}}\|_2^2] = (1 - \rho_b) \|\mathbf{F}_{\text{RF}} \mathbf{F}_{\text{BB}}\|_F^2 + \text{tr}(\mathbf{F}_{\text{RF}} \mathbf{R}_{ee} \mathbf{F}_{\text{RF}}^H)$ stands for the lossless transmitted signal power. In the appendix, we show that $P_{\tilde{x}} = P_{\max}$ when the baseband precoder presented in Section III-B is employed. Therefore, the actual transmitted power is $P_x = P_{\max}/L_{\text{RF}}$, satisfying the average power constraint. As discussed in Section II-D, the RF losses are not compensated for, reducing the actual transmit power and, consequently, the spectral efficiency.

This problem definition is sufficiently general to model other precoding schemes. For example, when $\rho_b = 0$, we have that $\mathbf{R}_{n_G n_G}^{-1/2} = \sigma_n^{-1} \mathbf{I}_{N_r}$, and the objective function is rewritten as $\log_2 \det \left(\mathbf{I}_{N_r} + \frac{1}{L_{\text{RF}}} \mathbf{R}_{n_G n_G}^{-1} \mathbf{H}_{\text{eq}} \mathbf{R}_{uu} \mathbf{H}_{\text{eq}}^H \right)$, which refers to the hybrid precoding problem [6] with lossy RF hardware. Moreover, when $\mathbf{F}_{\text{BB}} \in \mathbb{C}^{N_t \times N_s}$, $\mathbf{F}_{\text{RF}} = \mathbf{I}_{N_t}$, $L_{\text{RF}} = 1$, and $\rho_b = 0$, (13) falls back to the classical MIMO digital precoding problem. The corresponding quantized problems are obtained for $\rho_b \neq 0$.

To solve (13), we adopt the sub-optimal strategy of decoupling the precoder design problem into two subproblems for optimizing \mathbf{F}_{RF} and \mathbf{F}_{BB} , separately. We first tackle the analog precoding subproblem for obtaining \mathbf{F}_{RF} , allowing us to form the equivalent channel matrix \mathbf{H}_{eq} . Subsequently, we design our baseband precoder based on the SVD of \mathbf{H}_{eq} .

A. Analog Precoding Strategies

In the following, we present analog precoding methods for the fully- and partially-connected PSN topologies. Since \mathbf{F}_{RF} might have very large dimensions, the computational efforts of precoding design can be significant, and, thus, we focus on low computational complexity instead of high spectral efficiency.

1) *Fully-connected PSN*: As in [12], we design the RF precoder with the alternating projection method of [13, Section 3]. It consists of initially selecting the first L_t right singular vectors of the MIMO channel matrix \mathbf{H} and forming a semi-unitary precoder \mathbf{F}_{SU} . Next, this matrix is projected onto the unit-modulus space, and the result is projected back to the semi-unitary matrix \mathbf{F}_{SU} . This alternating projection procedure is repeated until convergence, which is achieved when the Frobenius norm residual between two consecutive iterations is smaller than a tolerance value. After convergence, the phase of each element in \mathbf{F}_{RF} is quantized to the closest value in the phase resolution set \mathcal{F}_{RF} . The fully-connected PSN hybrid precoder is summarized in Algorithm 1.

Algorithm 1 Hybrid precoding (fully-connected PSN)

Require: \mathbf{H} , L_t , b_{PS}

- 1: Compute SVD of $\mathbf{H} = \mathbf{U} \mathbf{\Sigma} \mathbf{V}^H$
- 2: Initialize $\mathbf{F}_{\text{SU}} \leftarrow [\mathbf{V}]_{:,1:L_t}$
- 3: **repeat**
- 4: $\mathbf{F}_{\text{RF}} \leftarrow \exp(j\angle \mathbf{F}_{\text{SU}})$
- 5: $\mathbf{F}_{\text{RF}} \xleftarrow{\text{SVD}} \mathbf{U} \mathbf{\Sigma} \mathbf{V}^H$
- 6: $\mathbf{F}_{\text{SU}} \leftarrow [\mathbf{U}]_{:,1:L_t} \mathbf{V}^H$
- 7: **until** convergence criterion triggers
- 8: $\mathbf{F}_{\text{RF}} \leftarrow \exp(j\mathcal{Q}_{b_{\text{PS}}}(\angle \mathbf{F}_{\text{RF}}))$

2) *Partially-connected PSN*: For the partially-connected RF precoding, we define the sub-channel matrix $\mathbf{H}_\ell =$

$[\mathbf{H}]_{:,n_a + (\ell-1)N_a} \in \mathbb{C}^{N_r \times N_a}$, $n_a = 1, \dots, N_a$, that contains the N_a columns of \mathbf{H} belonging to the ℓ -th antenna sub-array. The proposed design employs quantized MET for each sub-array, i.e., $\mathbf{f}_\ell = \exp(j\mathcal{Q}_{b_{\text{PS}}}(\angle \mathbf{v}_\ell^{\max}))$, $\ell = 1, \dots, L_t$, where \mathbf{v}_ℓ^{\max} denotes the right singular vector corresponding to the largest (dominant) singular value of \mathbf{H}_ℓ . The projection step enforces the unit-modulus constraint imposed by the phase-shifters. Since we are interested only in \mathbf{v}_ℓ^{\max} , we can use the simple power method to calculate it [21, Section 8.2.1]. This algorithm is significantly less expensive than, for example, the *R*-SVD algorithm which is useful for computing the full SVD. The power method achieves convergence when the residual error between two consecutive iterations is smaller than a tolerance value. It is guaranteed to converge if the dominant singular value is larger than all the other singular values in modulus and if the initial guess for \mathbf{v}_ℓ^{\max} has a non-zero component in the direction of the corresponding right singular vector [21], which occurs for the model presented in Section II-C. The partially-connected hybrid precoding method is outlined in Algorithm 2.

Algorithm 2 Analog beamforming for partially-connected PSN via the power method

Require: \mathbf{H} , L_t , N_a , b_{PS}

- 1: **for** $\ell = 1, \dots, L_t$ **do**
- 2: Form $\mathbf{H}_\ell \leftarrow [\mathbf{H}]_{:,n_a + (\ell-1)N_a}$, $n_a = 1, \dots, N_a$
- 3: Randomly initialize $\mathbf{v}_\ell \in \mathbb{C}^{N_a}$
- 4: **repeat**
- 5: $\mathbf{v}_\ell \leftarrow \mathbf{H}_\ell^H \mathbf{H}_\ell \mathbf{v}_\ell$
- 6: $\mathbf{v}_\ell \leftarrow \mathbf{v}_\ell / \|\mathbf{v}_\ell\|_2$
- 7: **until** convergence criterion triggers
- 8: $\mathbf{F}_{\text{RF}} \leftarrow \exp(j\mathcal{Q}_{b_{\text{PS}}}(\angle \mathbf{v}_\ell))$
- 9: **end for**

B. Digital Precoding Strategy

Unfortunately, finding the digital precoder \mathbf{F}_{BB} that maximizes (13) for fixed \mathbf{F}_{RF} is not straightforward. The SVD precoding with water-filling power allocation is not guaranteed anymore to decompose the MIMO system into orthogonal sub-channels due to the structure of the total noise vector \mathbf{n}' . Furthermore, in order to form \mathbf{H}' , one needs knowledge of the diagonal elements of \mathbf{R}_{uu} , which depends on \mathbf{F}_{BB} .

To solve these problems, notice that as the quantization resolution increases, $\rho_b \rightarrow 0$, $\mathbf{R}_{n_G n_G} \rightarrow \mathbf{R}_{nn}$, $\mathbf{H}' \rightarrow \mathbf{H}_{\text{eq}}$, and the instantaneous rate in (13) goes to $\log_2 \det \left(\mathbf{I}_{N_r} + \frac{1}{L_{\text{RF}}} \mathbf{R}_{nn}^{-1} \mathbf{H}_{\text{eq}} \mathbf{R}_{uu} \mathbf{H}_{\text{eq}}^H \right)$. In this case, SVD precoding and water-filling power allocation with respect to \mathbf{H}_{eq} and \mathbf{R}_{nn} become optimal. Note that this strategy still maximizes the achievable rate regardless of $\frac{1}{L_{\text{RF}}}$, thus we ignore this power loss factor in the transmitted signal model when designing \mathbf{F}_{BB} by setting $L_{\text{RF}} = 1$. In general, this strategy becomes sub-optimal under low-resolution quantization. Nevertheless, it is still expected to be close to optimal, particularly at low SNR. In such regime, AWGN overruns the quantization noise, motivating the use of the SVD precoding. At high SNR, however, the quantization noise dominates and this solution is only sub-optimal. Since massive MIMO systems will mostly operate in low SNR regimes, this choice is reasonable in practice.

Following our discussion, we design \mathbf{F}_{BB} as the optimal precoder in high-resolution scenarios. In this sense, we assume $\rho_b = 0$ and knowledge of \mathbf{F}_{RF} (see Section III-A), allowing \mathbf{H}_{eq} to be formed¹. The baseband precoder is then obtained by solving

$$\begin{aligned} \underset{\mathbf{F}_{\text{BB}}}{\text{maximize}} \quad & \log_2 \det (\mathbf{I}_{N_r} + \mathbf{R}_{nn}^{-1} \mathbf{H}_{\text{eq}} \mathbf{F}_{\text{BB}} \mathbf{F}_{\text{BB}}^H \mathbf{H}_{\text{eq}}^H) \\ \text{subject to} \quad & \mathbb{E} [\|\tilde{\mathbf{x}}\|_2^2] \leq P_{\max}. \end{aligned} \quad (14)$$

It is straightforward to show that the average power constraint in (14) can be rewritten as $\|\mathbf{F}_{\text{RF}} \mathbf{F}_{\text{BB}}\|_F^2 \leq P_{\max}$ when $\rho_b = 0$. Let the SVD of the equivalent channel be denoted by $\mathbf{H}_{\text{eq}} = \mathbf{U} \mathbf{\Sigma} \mathbf{V}^H$, in which $\mathbf{U} \in \mathbb{C}^{N_r \times N_s}$, $\mathbf{\Sigma} \in \mathbb{C}^{N_s \times N_s}$, and $\mathbf{V} \in \mathbb{C}^{M \times N_s}$. We employ SVD baseband precoding with water-filling power allocation, and normalize it so that the average power constraint in (14) is obeyed:

$$\mathbf{F}_{\text{BB}} = \frac{\sqrt{P_{\max}}}{\|\mathbf{F}_{\text{RF}} \mathbf{Q}\|_F} \mathbf{Q}, \quad (15)$$

where $\mathbf{Q} = \mathbf{V} \mathbf{\Lambda}^{1/2} \in \mathbb{C}^{N_t \times N_s}$ represents the SVD precoder with the diagonal power allocation matrix $\mathbf{\Lambda} \in \mathbb{R}^{N_s \times N_s}$. In the appendix, we show that the average power constraint is always satisfied regardless of DAC quantization resolution, and that $\|\mathbf{F}_{\text{RF}} \mathbf{Q}\|_F^2 = N_t P_{\max}$, which gives $\mathbf{F}_{\text{BB}} = \frac{1}{\sqrt{N_t}} \mathbf{Q}$.

For fully-digital transmitters, Problem (14) becomes

$$\begin{aligned} \underset{\mathbf{F}_{\text{BB}}}{\text{maximize}} \quad & \log_2 \det (\mathbf{I}_{N_r} + \mathbf{R}_{nn}^{-1} \mathbf{H} \mathbf{F}_{\text{BB}} \mathbf{F}_{\text{BB}}^H \mathbf{H}^H) \\ \text{subject to} \quad & \|\mathbf{F}_{\text{BB}}\|_F^2 \leq P_{\max}. \end{aligned}$$

The solution in this case is $\mathbf{F}_{\text{BB}} = \bar{\mathbf{V}} \bar{\mathbf{\Lambda}}^{-1/2}$, where $\bar{\mathbf{V}} \in \mathbb{C}^{N_t \times N_s}$ represents the right singular vector matrix of \mathbf{H} , and $\bar{\mathbf{\Lambda}} \in \mathbb{C}^{N_s \times N_s}$ the corresponding water-filling power allocation matrix.

C. Computational Complexity Analysis

The computational analysis of the proposed precoding methods is important to evaluate the impact of signal processing on the transmitter power budget with the power consumption modeling presented in Section II-D. In the following analysis, we consider that the matrix product of $\mathbf{A} \in \mathbb{C}^{M \times R}$ and $\mathbf{B} \in \mathbb{C}^{R \times N}$ requires $2MNR$ flops as in [21].

From our discussion in Section III-B, fully-digital precoding consists of SVD and water-filling power allocation. Its computational complexity is dominated by the algorithm that decomposes \mathbf{H} . According to [21, Figure 8.6.1], one needs $N_{\text{flops}}^{\text{SVD}} = 4P^2Q + 22Q^3$ flops to compute the full SVD of a $(P \times Q)$ -dimensional matrix with the R -SVD algorithm. Therefore, the number of flops necessary to obtain the digital precoder is $N_{\text{flops}}^{\text{D}} = 4N_r^2 N_t + 22N_t^3$.

Signal processing of hybrid precoding is carried out in two stages: baseband and analog precoding. The computational complexity of the former stage is dominated by the SVD of \mathbf{H}_{eq} which demands $N_{\text{flops}}^{\text{SVD}} = 4N_r^2 L_t + 22L_t^3 + 2N_r N_t L_t$ flops. The term $2N_r N_t L_t$ in $N_{\text{flops}}^{\text{SVD}}$ refers to the matrix product that forms \mathbf{H}_{eq} . The computational effort of the latter stage corresponds to the number of flops demanded by the analog

¹In a practical setup, \mathbf{H}_{eq} could be estimated at the receiver and sent back to via a feedback channel.

Table II: Flop counting for Algorithm 1.

Line	Flops count (per iteration)
4	$4N_t L_t$
5	$4N_t^2 L_t + 22L_t^3$
6	$2N_t L_t^2$

Table III: Flop counting for Algorithm 2.

Line	Flops count (per iteration)
5	$4N_t N_a$
6	$2N_a + 1$

precoding algorithm. The flop counting for Algorithms 1 and 2 is detailed in Tables II and III, respectively. According to Table II, $N_{\text{flops}}^{\text{PPSN}} = I(4N_t L_t + 4N_t^2 L_t + 22L_t^3 + 2N_t L_t^2)$ flops are necessary to compute the fully-connected analog precoder, where I denotes the number of iterations of the alternating minimization method. The total cost is then given by the baseband and analog precoders computation cost $N_{\text{flops}}^{\text{F}} = N_{\text{flops}}^{\text{SVD}} + N_{\text{flops}}^{\text{PPSN}}$. Note that in the computational cost of the fully-digital precoder $N_{\text{flops}}^{\text{D}}$, N_t is raised to the third power, whereas L_t is the cubic term in $N_{\text{flops}}^{\text{F}}$. This difference significantly reduces the hybrid precoder computational demands. According to Table III, the total number of flops necessary for computing the partially-connected analog precoder is $N_{\text{flops}}^{\text{PPSN}} = J(4N_t N_a + 2N_a + 1)$, where J represents the number of iterations of the power method. The total computation cost of the partially-connected hybrid precoder accounts for the calculation of \mathbf{H}_{eq} and its SVD. Therefore, it is given by $N_{\text{flops}}^{\text{P}} = N_{\text{flops}}^{\text{SVD}} + N_{\text{flops}}^{\text{PPSN}}$. Comparing $N_{\text{flops}}^{\text{F}}$ and $N_{\text{flops}}^{\text{P}}$, we observe that the latter is less complex than the former because the partially-connected structure is exploited to reduce the analog precoding computational complexity.

D. Achievable Rate Bounds

Now we conduct an asymptotic performance assessment of the quantized hybrid precoder. Let us consider the received signal model with Gaussian noise approximation and hybrid precoding: $\mathbf{y} \approx \frac{1}{L_{\text{RF}}} \mathbf{H}^H \mathbf{F}_{\text{BB}} \mathbf{s} + \mathbf{n}_G$, then we employ SVD combining (with respect to \mathbf{H}_{eq}) at the receiver, and finally decorrelate the Gaussian noise vector \mathbf{n}_G to obtain an achievable rate lower-bound. From Equation (15), it follows that the rotated received signal can be written as

$$\begin{aligned} \tilde{\mathbf{y}} &= \mathbf{U}^H \mathbf{y} = \frac{1}{\sqrt{L_{\text{RF}} N_t}} \mathbf{U}^H \mathbf{H}_{\text{eq}} \mathbf{\Upsilon}_b \mathbf{V} \mathbf{\Lambda}^{1/2} \mathbf{s} + \frac{1}{\sqrt{L_{\text{RF}}}} \mathbf{U}^H \mathbf{H}_{\text{eq}} \mathbf{e} + \mathbf{U}^H \mathbf{n} \\ &= \sqrt{\frac{1-\rho_b}{L_{\text{RF}} N_t}} \mathbf{\Sigma} \mathbf{\Lambda}^{1/2} \mathbf{s} + \tilde{\mathbf{n}}, \end{aligned}$$

where $\tilde{\mathbf{n}} = \frac{1}{\sqrt{L_{\text{RF}}}} \mathbf{\Sigma} \mathbf{V}^H \mathbf{e} + \mathbf{U}^H \mathbf{n} \in \mathbb{C}^{N_s}$ represents the rotated total additive Gaussian noise component with covariance matrix $\mathbf{R}_{\tilde{n}\tilde{n}} = \frac{1}{L_{\text{RF}}} \mathbf{\Sigma} \mathbf{V}^H \mathbf{R}_{ee} \mathbf{V} \mathbf{\Sigma} + \sigma_n^2 \mathbf{I}_{N_s}$. After the whitening filter, we have

$$\mathbf{R}_{\tilde{n}\tilde{n}}^{-1/2} \tilde{\mathbf{y}} = \sqrt{\frac{1-\rho_b}{L_{\text{RF}} N_t}} \mathbf{R}_{\tilde{n}\tilde{n}}^{-1/2} \mathbf{\Sigma} \mathbf{\Lambda}^{1/2} \mathbf{s} + \mathbf{R}_{\tilde{n}\tilde{n}}^{-1/2} \tilde{\mathbf{n}}.$$

This equation provides the following lower-bound for the achievable rate:

$$R \geq \log_2 \det \left(\mathbf{I}_{N_s} + \frac{1-\rho_b}{L_{\text{RF}} N_t} \mathbf{R}_{\tilde{n}\tilde{n}}^{-1/2} \mathbf{\Sigma} \mathbf{\Lambda} \mathbf{\Sigma} \mathbf{R}_{\tilde{n}\tilde{n}}^{-1/2, \text{H}} \right). \quad (16)$$

For low-resolution quantization and high SNR, water-filling power allocation yields $\mathbf{\Lambda} = (P_{\max}/N_s) \mathbf{I}_{N_s}$ and (16) goes to

$$R \geq \log_2 \det \left(\mathbf{I}_{N_s} + \frac{P_{\max}(1-\rho_b)}{L_{\text{RF}} N_t N_s} \mathbf{R}_{\text{high}}^{-1/2} \mathbf{\Sigma}^2 \mathbf{R}_{\text{high}}^{-1/2, \text{H}} \right), \quad (17)$$

where $\mathbf{R}_{\text{high}} = \mathbf{\Sigma} \mathbf{V}^H \mathbf{R}_{ee} \mathbf{V} \mathbf{\Sigma}$. At low SNR, the achievable rate is lower bounded by $R \geq \log_2 \left[1 + (1-\rho_b) \frac{\gamma}{L_{\text{RF}} N_t} \sigma_{\max}^2 \right]$. Inequality (17) shows that quantization noise dominates over AWGN in high SNR regime, leading to saturation of the system capacity. The obtained achievable rate expression at low SNR shows that quantized system capacity is always smaller than that of unquantized systems due to the factor $(1-\rho_b)$ inside the logarithm.

IV. SIMULATION RESULTS

In this section, we present the results of numerical simulations conducted to evaluate the spectral and energy efficiencies of the proposed precoding strategies. Also, the power consumption model introduced in Section II-D is assessed. Hereafter, hybrid precoding with fully- and partially-connected PSN are referred to as HPF and HPP, respectively. The obtained results are averaged over 1000 independent experiments. For each experiment realization, a channel matrix with $L = 5$ paths is generated according to Equation (10). We set the average transmit power constraint to $P_{\max} = 1\text{W}$, which is reasonable for base stations with small coverage. Also, in order to reduce costs, the number L_t of RF chains is equal to the number of streams. We assume phase-shifters with phase range of 360° and shift resolution of $b_{\text{PS}} = 5$ bits, as in the hardware implementation of [30]. The DAC sampling rate is set to $F_s = 1\text{GHz}$, which should be sufficient for mmWave systems to provide high data rates. Regarding the calculation of computational power consumption, we consider the same parameters as in [20]: computational efficiency of $E_c = 12.8\text{ Gflops/s/W}$, channel coherence bandwidth of $B_C = 180\text{ kHz}$, and channel coherence time of $T_C = 10\text{ ms}$, giving $C = B_C T_C = 1800$ coherence blocks per second. The convergence tolerance of the iterative algorithms is defined as 10^{-6} . Preliminary simulations have shown that the iterative algorithms used to compute HPF and HPP converge within 40 and 13 iterations on average, respectively.

A. Spectral Efficiency

Figures 2, 3, and 4 show the spectral efficiency of the digital and hybrid precoders as function of the SNR for DAC resolution of 1 and 8 bits. The curves depicted in Figure 2 indicate that the quantized digital precoder does not lose much spectral efficiency at low SNR, whereas its performance saturates at high SNR. This is because quantization distortion does not drop at high SNR, as discussed in Section III-D. Since the distortion caused by 1-bit DACs is important, the spectral efficiency already saturates at 16 dB, whereas it occurs only at $> 40\text{ dB}$ for 8-bit DACs. The spectral efficiency

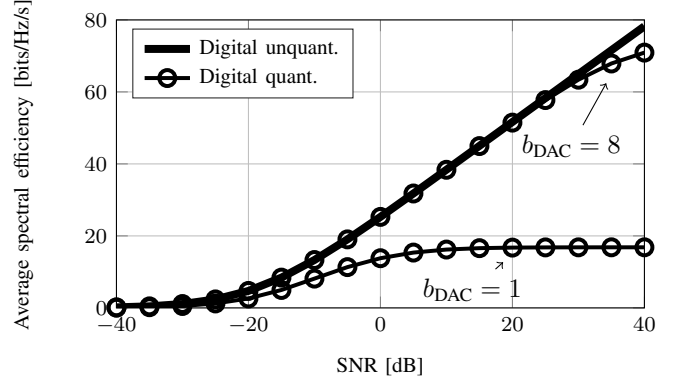


Fig. 2: Spectral efficiency of digital precoders. $N_t = 64$, $N_r = 32$, $L_t = N_s = 4$, $b_{\text{DAC}} \in \{1, 8\}$.

of lossless hybrid precoders using active and passive phase-shifters is compared to that of the unquantized digital precoder in Figure 3. As observed in several hybrid precoding works, HPF performs better than HPP when RF hardware losses are ignored. In this case, the type of phase-shifting circuit does not have any impact on the spectral efficiency as no insertion losses are considered yet. Comparing Figures 2 and 3 one recognizes that hybrid precoding saturates at lower data rates compared to digital precoding. This is because the quantization distortion e is filtered by analog precoding matrix \mathbf{F}_{RF} , as visible in Equation (5), increasing the total noise \mathbf{n}' power. In general, digital precoding provides higher data rate than hybrid precoding for fixed number of bits per DAC and SNR values.

In Figure 4, the performance of the hybrid precoders is shown considering RF hardware losses. In this scenario, HPF performs worse than HPP because its insertion loss is larger than that of the other architecture, which causes smaller effective transmit power, and spectral efficiency. When RF losses are taken into account, the phase-shifting implementation becomes important. As shown in Figure 4, precoders with active phase-shifters are more spectral-efficient since these components present smaller insertion loss compared to passive phase-shifters, however they come with increased power consumption. SNR losses of 25 dB observed in Figure 4 have also been reported in other works [10], [42]. Such large losses occur due to the very large number of lossy RF components employed in the massive MIMO setup.

B. Power Consumption

The static power consumption is plotted as function of the number N_t of antennas for $b_{\text{DAC}} \in \{1, 3, 5, 7\}$ in the left part of Figure 5. Despite the reduced number of RF chains, HPF with active phase-shifters can be still very power hungry, even more than the digital precoder. This is mainly due to the power consumption of the fully-connected PSN. To solve this issue, one can employ passive phase-shifters, drastically decreasing the power demand of the PSN as shown in Figure 5. However, as observed in Figure 4, the use of such passive components implies spectral efficiency degradation. One can also observe

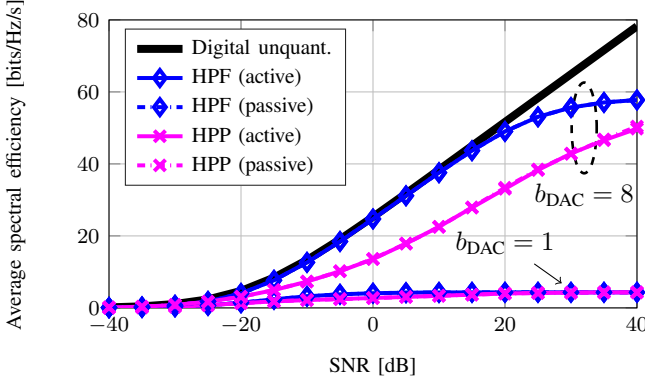


Fig. 3: Spectral efficiency of hybrid precoders (ignoring RF hardware losses). $N_t = 64$, $N_r = 32$, $L_t = N_s = 4$, $b_{\text{DAC}} \in \{1, 8\}$.

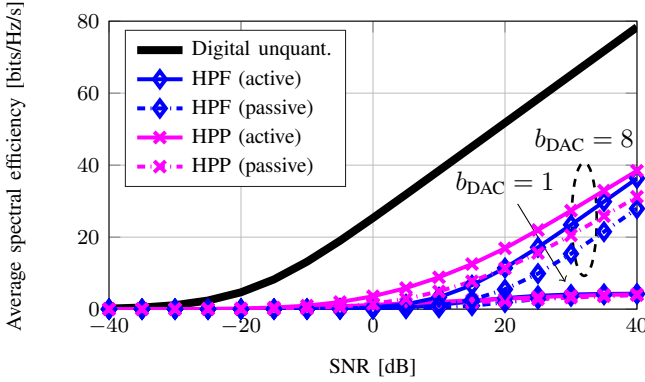


Fig. 4: Spectral efficiency of hybrid precoders (considering RF hardware losses). $N_t = 64$, $N_r = 32$, $L_t = N_s = 4$, $b_{\text{DAC}} \in \{1, 8\}$.

the effect of DAC resolution on the static power consumption. Digital precoding is more sensitive to DAC resolution because it uses N_t DACs, while hybrid precoding uses only L_t .

In practice, computational power consumption plays an important role on system energy efficiency. The plot in the right part of Figure 5 suggests that it is negligible when the antenna array is comparatively small (up to 128 antennas). By contrast, it becomes substantial for HPF and digital precoder with growing N_t . HPP is not as power hungry since the number of flops necessary to run Algorithm 2 scales linearly with the number N_t of transmitting antennas, whereas the other schemes contain quadratic and cubic terms of N_t . Although both schemes rely on the SVD for computing the baseband filter, the fully-digital approach decomposes an $(N_r \times N_t)$ -dimensional total channel matrix, while hybrid approaches factorize an $(N_r \times L_t)$ -dimensional matrix. Since $L_t \ll N_t$, the SVD of the former is more expensive than that of the latter. We stress that the proposed power consumption model mainly serves to provide energy efficiency estimates, allowing us to compare different precoding structures. In practice, optimized hardware and software designs may reduce the values provided by our model. For example, one can simplify PA, DAC, and modulation design when employing 1-bit quantization.

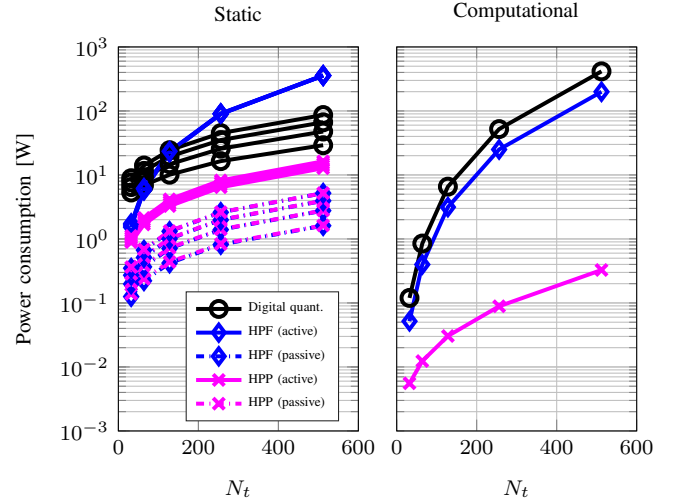


Fig. 5: $N_r = 32$, $L_t = N_s$, $b_{\text{DAC}} \in \{1, 3, 5, 7\}$, $(N_t, N_s) \in \{(32, 2), (64, 4), (128, 8), (256, 16), (512, 32)\}$.

However, considering such specialized implementations is out of the scope of this work.

C. Energy Efficiency

Numerical experiments were also carried out to study the energy efficiency of the proposed precoding strategies and its trade-off with spectral efficiency. The compromise between active and passive phase-shifters is investigated as well. Mathematically, energy efficiency is defined as $EE = R_m/P_m$ [20] for $m \in \{\text{Dig, FPSN, PPSN}\}$. Figure 6 shows energy-spectral efficiency curves for varying DAC resolution. A system designer should aim at maximizing both figures of merit, approaching the top right corner of the chart in Figure 6.

In contrast to what is usually claimed by several hybrid precoding papers, Figure 6 indicates that HPF is the least efficient precoding method. This is because the insertion losses associated with RF hardware (especially power dividers and combiners) drastically reduce its throughput, which results in energy efficiency degradation. Such losses are disregarded in most hybrid precoding works, leading to the erroneous conclusion that fully-connected PSN is the most spectral-efficient topology in general. As an alternative to HPF, transmitters equipped with partially-connected PSNs lose less power as they use a smaller number of phase-shifters and power dividers. Therefore, as observed in Figure 6, HPP can be more energy-efficient than HPF. This figure also reveals that phase-shifter topology offers an energy-spectral efficiency trade-off. As active phase-shifting exhibits small insertion loss and non-negligible power consumption, it favors spectral efficiency. On the other hand, passive phase-shifting causes important power loss, but offers negligible power consumption, promoting energy efficiency. Among the studied precoding methods, digital precoding is the most spectral-efficient solution for obvious reasons. According to Figure 4, hybrid precoding exhibits poor throughput performance in low SNR compared to digital precoding, shifting upwards the curve of the latter method. Therefore, digital precoding can be the

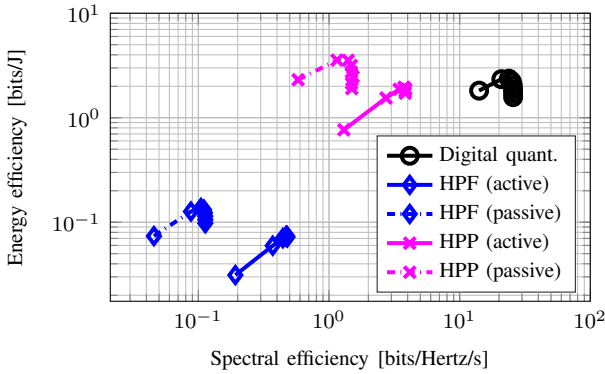


Fig. 6: Energy-spectral efficiency curves for varying DAC resolution. $N_t = 64$, $N_r = 32$, $L_t = N_s = 4$, SNR = 0 dB, $b_{\text{DAC}} \in \{1, \dots, 8\}$.

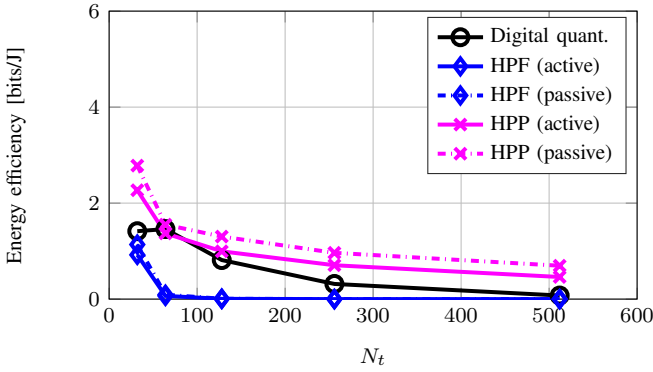


Fig. 7: SNR = 0 dB, $b_{\text{DAC}} = 3$, and $(N_t, N_s) \in \{(32, 2), (64, 4), (128, 8), (256, 16), (512, 32)\}$, $L_t = N_s$.

most energy-efficient method in low SNR regime. Regarding DAC resolution, Figure 6 also shows that using $b_{\text{DAC}} > 3$ does not necessarily increase efficiency and may even lead to performance degradation.

Do the results obtained from Figure 6 hold for other scenarios? More specifically, do they still hold for transmitting arrays with more antenna elements? To answer these questions, consider Figures 7 and 8, where energy efficiency is plotted for different (N_t, N_s) tuples at high and low SNR, respectively. These plots were obtained by setting $b_{\text{DAC}} = 3$, motivated by the discussion above. At high SNR, HPP with passive phase-shifters is the most energy-efficient scheme even for transmitting arrays with 512 antennas. At low SNR, however, digital precoding is the most energy-efficient solution up to 350 antennas. This result motivates the adoption of hybrid systems in environments where the SNR is typically high, such as indoor scenarios where line of sight propagation usually occurs.

V. CONCLUSION

Hybrid precoding with fully-connected PSN exhibits important power losses mostly due to the large number of phase-shifters, power dividers and combiners used in the massive MIMO setup. Such power loss is not easily compensated with

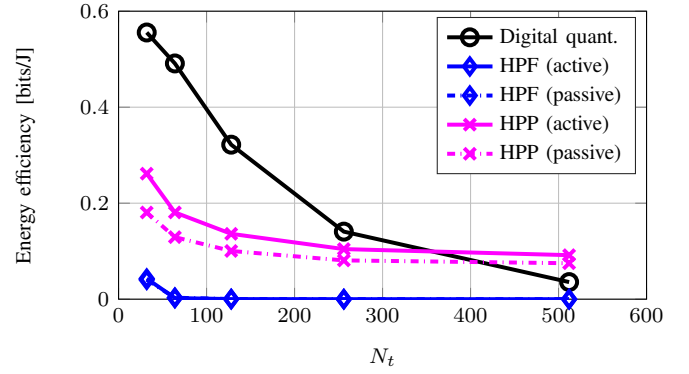


Fig. 8: SNR = -15 dB, $b_{\text{DAC}} = 3$, and $(N_t, N_s) \in \{(32, 2), (64, 4), (128, 8), (256, 16), (512, 32)\}$, $L_t = N_s$.

present mmWave PA technology, causing severe spectral and energy efficiency degradation. As an alternative, hybrid precoders equipped with partially-connected PSN are shown to be energy-efficient in high SNR regimes. Our results revealed that phase-shifting topology offers an energy-spectral efficiency trade-off. Active phase-shifters favor higher throughput, while passive elements aim at energy efficiency. Finally, the proposed power consumption model suggests that computational power spending should be considered in the power budget of very-large array systems. The present work considered a point-to-point MIMO system for simplicity reasons. Introducing interfering users, performing transceiver optimization, and designing efficient hybrid schemes are envisioned as future work.

APPENDIX

We demonstrate that the power of the lossless transmitted signal with DAC approximation (5) follows the average power constraint for hybrid precoding. This power is defined as $P_{\bar{x}} = \mathbb{E} [\|\bar{x}\|_2^2] = \text{tr}(\mathbf{F}_{\text{RF}} \mathbf{Y}_b \mathbf{F}_{\text{BB}} \mathbf{F}_{\text{BB}}^H \mathbf{Y}_b \mathbf{F}_{\text{RF}}^H) + \text{tr}(\mathbf{F}_{\text{RF}} \mathbf{R}_{ee} \mathbf{F}_{\text{RF}}^H)$. From Equation (6), it follows that $P_{\bar{x}}$ can be rewritten as $P_{\bar{x}} \approx (1 - \rho_b) \|\mathbf{F}_{\text{RF}} \mathbf{F}_{\text{BB}}\|_F^2 + \rho_b \text{tr}(\mathbf{F}_{\text{RF}} \text{diag}(\mathbf{F}_{\text{BB}} \mathbf{F}_{\text{BB}}^H) \mathbf{F}_{\text{RF}}^H)$. We need to calculate the diagonal matrix $\text{diag}(\mathbf{F}_{\text{BB}} \mathbf{F}_{\text{BB}}^H)$. To do so, consider $\mathbf{A} = \theta \mathbf{I}_M$. One can readily see that $\text{diag}(\mathbf{A}) = \text{Diag}([\text{tr}(\mathbf{A})/M, \dots, \text{tr}(\mathbf{A})/M])$. Although the diagonal elements of $\mathbf{F}_{\text{BB}} \mathbf{F}_{\text{BB}}^H$ are not necessarily equal, they should be similar due to power allocation, yielding the following approximation $\text{diag}(\mathbf{F}_{\text{BB}} \mathbf{F}_{\text{BB}}^H) \approx \text{Diag}(\text{tr}(\mathbf{F}_{\text{BB}} \mathbf{F}_{\text{BB}}^H)/L_t, \dots, \text{tr}(\mathbf{F}_{\text{BB}} \mathbf{F}_{\text{BB}}^H)/L_t) \approx \|\mathbf{F}_{\text{BB}}\|_F^2 / L_t$. This estimate gives $P_{\bar{x}} \approx (1 - \rho_b) \|\mathbf{F}_{\text{RF}} \mathbf{F}_{\text{BB}}\|_F^2 + \rho_b \frac{\|\mathbf{F}_{\text{BB}}\|_F^2 \|\mathbf{F}_{\text{RF}}\|_F^2}{L_t}$. The baseband precoder normalization (15) leads to $\|\mathbf{F}_{\text{BB}}\|_F^2 = \frac{P_{\max}}{\|\mathbf{F}_{\text{RF}} \mathbf{Q}\|_F^2} \text{tr}(\mathbf{Q} \mathbf{Q}^H)$. From water-filling power allocation, $\text{tr}(\mathbf{Q} \mathbf{Q}^H) = P_{\max}$, and the denominator can be written as $\|\mathbf{F}_{\text{RF}} \mathbf{Q}\|_F^2 = \text{tr}(\mathbf{F}_{\text{RF}} \mathbf{V} \Lambda \mathbf{V}^H \mathbf{F}_{\text{RF}}^H)$. Notice we can approximate $\mathbf{Q} \mathbf{Q}^H \approx \frac{P_{\max}}{L_t} \mathbf{I}_{L_t}$, therefore $\|\mathbf{F}_{\text{RF}} \mathbf{Q}\|_F^2 \approx \frac{P_{\max}}{L_t} \text{tr}(\mathbf{F}_{\text{RF}} \mathbf{F}_{\text{RF}}^H) = N_t P_{\max}$. We finally get $\|\mathbf{F}_{\text{BB}}\|_F^2 = P_{\max} / N_t$ and $P_{\bar{x}} \approx [(1 - \rho_b) + \rho_b] P_{\max} = P_{\max}$. This result can be easily extended to digital precoding by making $\mathbf{F}_{\text{BB}} \in \mathbb{C}^{N_t \times N_s}$ and $\mathbf{F}_{\text{RF}} = \mathbf{I}_{N_t}$.

REFERENCES

[1] C.-X. Wang, F. Haider, X. Gao, X.-H. You, Y. Yang, D. Yuan, H. Aggoun, H. Haas, S. Fletcher, and E. Hepsaydir, "Cellular architecture and key technologies for 5G wireless communication networks," *IEEE Communications Magazine*, vol. 52, no. 2, pp. 122–130, Feb. 2014.

[2] J. G. Andrews, S. Buzzi, W. Choi, S. V. Hanly, A. Lozano, A. C. K. Soong, and J. C. Zhang, "What will 5G be?" *IEEE Journal on Selected Areas in Communications*, vol. 32, no. 6, pp. 1065–1082, Jun. 2014.

[3] E. G. Larsson, O. Edfors, F. Tufvesson, and T. L. Marzetta, "Massive MIMO for next generation wireless systems," *IEEE Communications Magazine*, vol. 52, no. 2, pp. 186–195, Feb. 2014.

[4] S. Schwarz and M. Rupp, "Society in motion: challenges for LTE and beyond mobile communications," *IEEE Communications Magazine*, vol. 54, no. 5, pp. 76–83, May 2016.

[5] R. W. Heath, "Millimeter wave: the future of commercial wireless systems," in *Proc. 2016 IEEE Compound Semiconductor Integrated Circuit Symposium (CSICS)*, Austin, TX, USA, Oct. 2016, pp. 1–4.

[6] O. El Ayach, S. Rajagopal, S. Abu-Surra, Z. Pi, and R. W. Heath, "Spatially sparse precoding in millimeter wave MIMO systems," *IEEE Transactions on Wireless Communications*, vol. 13, no. 3, pp. 1499–1513, Mar. 2014.

[7] R. W. Heath, N. Gonzalez-Prelcic, S. Rangan, W. Roh, and A. M. Sayeed, "An overview of signal processing techniques for millimeter wave mimo systems," *IEEE Journal of Selected Topics in Signal Processing*, vol. 10, no. 3, pp. 436–453, Apr. 2016.

[8] R. Méndez-Rial, C. Rusu, N. González-Prelcic, A. Alkhateeb, and R. W. Heath, "Hybrid MIMO architectures for millimeter wave communications: Phase shifters or switches?" *IEEE Access*, vol. 4, pp. 247–267, 2016.

[9] C. Tsinos, S. Maleki, S. Chatzinotas, and B. Ottersten, "On the energy-efficiency of hybrid analog-digital transceivers for single-and multi-carrier large antenna array systems," *IEEE Journal on Selected Areas in Communications*, vol. 35, no. 9, pp. 1980–1995, Sep. 2017.

[10] A. Garcia-Rodriguez, V. Venkateswaran, P. Rulikowski, and C. Masiouros, "Hybrid analogdigital precoding revisited under realistic RF modeling," *IEEE Wireless Communications Letters*, vol. 5, no. 5, pp. 528–531, Oct. 2016.

[11] O. Orhan, E. Erkip, and S. Rangan, "Low power analog-to-digital conversion in millimeter wave systems: Impact of resolution and bandwidth on performance," in *Proc. Information Theory and Applications Workshop (ITA), 2015*. San Diego, CA, USA: IEEE, 2015, pp. 191–198.

[12] W. b. Abbas, F. Gomez-Cuba, and M. Zorzi, "Millimeter wave receiver efficiency: a comprehensive comparison of beamforming schemes with low resolution ADCs," *arXiv preprint arXiv:1607.03725*, 2016.

[13] J. A. Tropp, I. S. Dhillon, R. W. Heath, and T. Strohmer, "Designing structured tight frames via an alternating projection method," *IEEE Transactions on Information Theory*, vol. 51, no. 1, pp. 188–209, Jan. 2005.

[14] K. Roth and J. A. Nossek, "Achievable rate and energy efficiency of hybrid and digital beamforming receivers with low resolution ADC," *arXiv preprint arXiv:1610.02909*, 2016.

[15] T. L. Marzetta, E. G. Larsson, H. Yang, and H. Q. Ngo, *Fundamentals of Massive MIMO*. Cambridge University Press, 2016.

[16] L. N. Ribeiro, S. Schwarz, M. Rupp, A. L. F. de Almeida, and J. C. M. Mota, "A Low-Complexity Equalizer for Massive MIMO Systems Based on Array Separability," in *Proc. 2017 25th European Signal Processing Conference (EUSIPCO 2017)*, Kos, Greece, Aug. 2017, pp. 2522–2526.

[17] A. Mezghani, R. Ghiat, and J. A. Nossek, "Transmit processing with low resolution D/A-converters," in *Proc. 16th IEEE International Conference on Electronics, Circuits, and Systems (ICECS 2009)*, Yasmine Hammamet, Tunisia, 2009, pp. 683–686.

[18] J. J. Bussgang, "Crosscorrelation functions of amplitude-distorted Gaussian signals," 1952.

[19] S. Jacobsson, G. Durisi, M. Coldrey, T. Goldstein, and C. Studer, "Quantized precoding for massive MU-MIMO," *arXiv preprint arXiv:1610.07564*, 2016.

[20] E. Björnson, L. Sanguinetti, J. Hoydis, and M. Debbah, "Optimal design of energy-efficient multi-user MIMO systems: Is massive MIMO the answer?" *IEEE Transactions on Wireless Communications*, vol. 14, no. 6, pp. 3059–3075, Jun. 2015.

[21] G. H. Golub and C. F. Van Loan, *Matrix computations*. JHU Press, 2012, vol. 3.

[22] F. Sohrabi and W. Yu, "Hybrid beamforming with finite-resolution phase shifters for large-scale MIMO systems," in *Proc. IEEE 16th International Workshop on Signal Processing Advances in Wireless Communications (SPAWC)*, Stockholm, Sweden, Jul. 2015, pp. 136–140.

[23] J. Max, "Quantizing for minimum distortion," *IRE Transactions on Information Theory*, vol. 6, no. 1, pp. 7–12, Mar. 1960.

[24] J. Makhoul, S. Roucos, and H. Gish, "Vector quantization in speech coding," *Proceedings of the IEEE*, vol. 73, no. 11, pp. 1551–1588, Nov. 1985.

[25] A. Mezghani and J. A. Nossek, "Capacity lower bound of MIMO channels with output quantization and correlated noise," in *Proc. IEEE International Symposium on Information Theory Proceedings (ISIT)*, Cambridge, MA, USA, Jul. 2012.

[26] S. N. Diggavi and T. M. Cover, "The worst additive noise under a covariance constraint," *IEEE Transactions on Information Theory*, vol. 47, no. 7, pp. 3072–3081, Nov. 2001.

[27] W. Yu, W. Rhee, S. Boyd, and J. M. Cioffi, "Iterative water-filling for Gaussian vector multiple-access channels," *IEEE Transactions on Information Theory*, vol. 50, no. 1, pp. 145–152, Jan. 2004.

[28] Z. Gao, L. Dai, D. Mi, Z. Wang, M. A. Imran, and M. Z. Shakir, "mmWave massive-MIMO-based wireless backhaul for the 5G ultra-dense network," *IEEE Wireless Communications*, vol. 22, no. 5, pp. 13–21, Oct. 2015.

[29] E. Zöchmann, M. Lerch, S. Caban, C. F. Mecklenbräuker, and M. Rupp, "Directional evaluation of receive power, Rician K-factor and RMS delay spread obtained from power measurements of 60 GHz indoor channels," in *Proc. IEEE APS Topical Conference on Antennas and Propagation in Wireless Communications (APWC)*, Cairns, QLD, Australia, 2016, pp. 246–249.

[30] D. Huang, L. Zhang, L. Zhang, and Y. Wang, "A 60 GHz 360° 5-bit digitally controlled high-pass/direct-pass T-type phase shifter using nMOS body-floating switch," *Analog Integrated Circuits and Signal Processing*, vol. 90, no. 1, pp. 93–100, Jan. 2017.

[31] K. S. V. Prasad, E. Hossain, and V. K. Bhargava, "Energy efficiency in massive MIMO-based 5G networks: Opportunities and challenges," *IEEE Wireless Communications*, vol. 24, no. 3, pp. 86–94, 2017.

[32] C. Marcu, "LO Generation and Distribution for 60 GHz Phased Array Transceivers," Ph.D. dissertation, EECS Department, University of California, Berkeley, 2011. [Online]. Available: <http://www2.eecs.berkeley.edu/Pubs/TechRpts/2011/EECS-2011-132.html>

[33] Y. Jin, J. R. Long, and M. Spirito, "A 7 dB NF 60 GHz-band millimeter-wave transconductance mixer," in *Proc. 2011 IEEE Radio Frequency Integrated Circuits Symposium (RFIC)*, Baltimore, MD, USA, 2011, pp. 1–4.

[34] S. Rangan, T. Rappaport, E. Erkip, Z. Latinovic, M. R. Akdeniz, and Y. Liu, "Energy efficient methods for millimeter wave picocellular systems," in *Proc. IEEE Communications Theory Workshop*, Phuket, Thailand, Jun. 2013, pp. 1–25.

[35] K. Scheir, S. Bronckers, J. Borremans, P. Wambacq, and Y. Rolain, "A 52 GHz phased-array receiver front-end in 90 nm digital CMOS," *IEEE Journal of Solid-State Circuits*, vol. 43, no. 12, pp. 2651–2659, Dec. 2008.

[36] S. Cui, A. J. Goldsmith, and A. Bahai, "Energy-constrained modulation optimization," *IEEE Transactions on Wireless Communications*, vol. 4, no. 5, pp. 2349–2360, Sep. 2005.

[37] E. Olieman, "Time-interleaved high-speed D/A converters," Ph.D. dissertation, University of Twente, 2016. [Online]. Available: <http://doc.utwente.nl/99674/>

[38] K. Gao, N. J. Estes, B. Hochwald, J. Chisum, and J. N. Laneman, "Power-performance analysis of a simple one-bit transceiver," in *Proc. 2017 Information Theory and Applications Workshop (ITA)*, San Diego, CA, USA, Feb. 2017, pp. 1–10.

[39] K. Greene, A. Sarkar, and B. Floyd, "A 60-GHz Dual-Vector Doherty Beamformer," *IEEE Journal of Solid-State Circuits*, vol. 52, no. 5, pp. 1373–1387, May 2017.

[40] D. Pepe and D. Zito, "A 78.8–92.8 GHz 4-bit 0–360° active phase shifter in 28nm FDSOI CMOS with 2.3 dB average peak gain," in *Proc. 41st European Solid-State Circuits Conference (ESSCIRC)*, Graz, Austria, Sep. 2015, pp. 64–67.

[41] E. Biglieri, R. Calderbank, A. Constantinides, A. Goldsmith, A. Paulraj, and H. V. Poor, *MIMO Wireless Communications*. Cambridge university press, 2007.

[42] E. Zöchmann, S. Schwarz, and M. Rupp, "Comparing antenna selection and hybrid precoding for millimeter wave wireless communications," in *Proc. 2016 IEEE Sensor Array and Multichannel Signal Processing Workshop (SAM)*, Rio de Janeiro, Brazil, 2016, pp. 1–5.